Journal of Alloys and Compounds 509 (2011) 4404–4413

Contents lists available at ScienceDirect

Journal of Alloys and Compounds

journal homepage: www.elsevier.com/locate/jallcom

Magnetic properties of thermal plasma synthesized nanocrystalline nickel ferrite ($NiFe_2O_4$)

Ashok B. Nawale [a], Nilesh S. Kanhe [a], K.R. Patil [b], S.V. Bhoraskar [a], V.L. Mathe [a,*], A.K. Das [c]

[a] Department of Physics, University of Pune, Ganeshkhind, Pune 411007, India
[b] Center for Materials Characterizations, National Chemical Laboratory, Dr. Homi Bhabha Road, Pashan, Pune 411008, India
[c] Laser and Plasma Technology Division, Bhabha Atomic Research Centre, Trombay, Mumbai 400085, India

ARTICLE INFO

Article history:
Received 18 September 2010
Received in revised form 5 January 2011
Accepted 8 January 2011
Available online 15 January 2011

Keywords:
Nanostructured materials
Magnetization
Crystal structure
Magnetic measurements
TEM

ABSTRACT

A rapid synthesis method is reported for magnetic nanoparticles of nickel ferrite involving thermal plasma assisted vapor phase condensation process. The as-synthesized samples were characterized by X-ray Diffraction, Transmission Electron Microscopy, Vibrating Sample Magnetometer and X-ray Photoelectron Spectroscopy techniques. The average particle size was determined from the TEM micrographs and found to be around 30 nm. The effects of reactor parameters on the magnetic and structural properties have been evaluated, to find the optimized parameters so as to achieve the highest values of saturation magnetization and coercivity. Reasonably high saturation magnetization (48 emu/g) has been assigned to the high degree of crystallinity, achieved on account of high temperature during the growth, and the cation redistribution. The high value of coercivity (115 Oe) is explained on the basis of possible lattice defects arising from the cation redistribution. Detailed analysis of cation distribution using the XRD line intensity data leads to the conclusion that these samples are iron deficit and nickel rich.

1. Introduction

The importance of the nanocrystalline spinel ferrites with the general formula AFe_2O_4 (A = Mn, Co, Ni, Cu or Zn) is well known due to their interesting magnetic and electrical properties on account of chemical and thermal stabilities. These materials are technologically important and have been used in many applications. These include magnetic recording media, magnetic fluids for the storage or retrieval of information, magnetic resonance imaging (MRI) enhancement, catalysis, magnetically guided drug delivery, microwave absorber and sensors and pigments [1,2].

Nickel ferrite ($NiFe_2O_4$) is one of the most important spinel ferrites. It has an inverse spinel structure showing ferrimagnetism that originates from magnetic moment of anti-parallel spins between Fe^{3+} ions at tetrahedral sites and Ni^{2+}, Fe^{3+} ions at octahedral sites [3]. Powder of nanosize nickel ferrite is useful as ferro-fluids, radar-absorbing coating and biomedical material [4]. Looking at such diverse applications it is always advantageous to explore new processes which can yield massive production of non agglomerated nanoparticles with good magnetic properties.

Large scale synthesis of nanomaterials of varieties of metals, metal oxides and nitrides using thermal arc plasma assisted gas phase synthesis, has gained importance in the recent years [5]. Thermal plasma processing gives the clean reaction atmosphere which is required for the high purity materials. It provides high enthalpy which increases the reaction kinetics by several orders of magnitude and steep temperature gradient that enables rapid quenching and generation of the fine particles [6]. Due to such inherent advantages, thermal plasma processing has become a very useful technique for producing new kinds of nanomaterials. Earlier we have reported the synthesis of various kinds of nanomaterials including those of aluminum, titanium oxide, aluminum oxide, iron oxide, aluminum nitride and silicon using this method [7–10]. However synthesis of mixed oxide nanophase materials has yet to be realized using this novel technique. Although Reddy et al. have reported the synthesis of different alloys using thermal plasma route [6], very few attempts have been made to grow the nanomaterials of binary or ternary oxides.

On account of its potential applications in the large scale production of highly crystalline nanomaterials we have made an attempt to grow nanocrystalline nickel ferrite by gas phase reaction of nickel and iron with oxygen. This method has the advantage that no post calcination is required to achieve the required crystalline phase, as in the conventional chemical routes. This is so because the plasma excited at near atmospheric pressure, as is necessary in the present case, maintains the local thermodynamic equilibrium within the plasma jet. Subsequently the thermal energy is transferred to the anode (metal to be evaporated) and the vapors from the target metal are ejected and they encounter collisions with the oxygen species near the boundaries of the plasma jet. As the

* Corresponding author. Tel.: +91 020 25692678; fax: +91 020 25691684.
E-mail address: vlmathe@physics.unipune.ac.in (V.L. Mathe).

0925-8388/$ – see front matter © 2011 Elsevier B.V. All rights reserved.
doi:10.1016/j.jallcom.2011.01.057

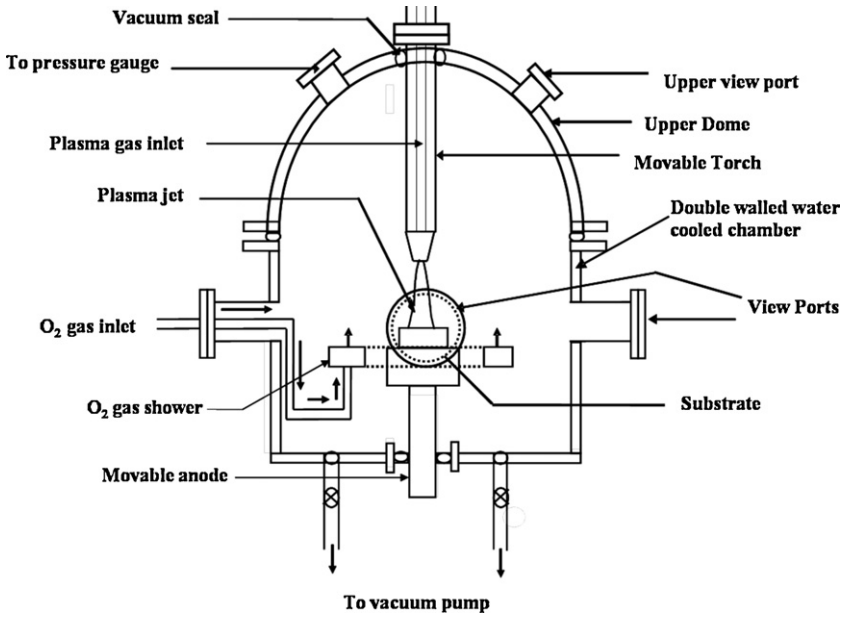

Fig. 1. Schematic of the direct current transferred arc thermal plasma reactor.

appropriate supercooling is achieved, nuclei begin to form in the gas phase. Growth occurs when these nuclei interact with further gaseous species. However, due to the excessive collisions, the reaction product cools down and the growth gets arrested. This process of homogeneous nucleation, resulting from vapor–vapor interface reactions, is quite complicated in a mixed oxide system. This will be more stringent if the melting points of the constituents differ largely. Moreover the oxidation rates of the two metals may also be significantly different. In such cases one of the oxides can precipitate more in the mixed product leading to a non stoichiometric compound. It is also possible that, due to the rapid quenching process, the metal ions can enter into the anti-sites leading to the formation of defects. Properties of multi-component ferrite are quite sensitive to these anti-site defects and therefore it is necessary to generate experimental data and optimize the reaction parameters in such thermal plasma reactor. In spite of such complexity this process has the advantage that one can synthesize the nanomaterials in a short duration of time. This rapid method can be compared with the conventional methods which are used for the synthesis of $NiFe_2O_4$ [3,4,11–26] or other mixed oxides. Among these established methods, it is critical to find a simple and quick route to synthesize nanocrystalline $NiFe_2O_4$ by utilizing cheap, nontoxic and environmentally benign precursors. All these methods require a prolonged (>10 h) heat treatment for obtaining the required phase transformation. Also the literature shows that the properties of the ferrite nano particles strongly depend on the process parameters.

In this paper we have made an attempt to synthesize the nano particles of nickel ferrite at different operating pressures and different plasma powers. The primary assessment was based on the measured values of magnetization and the X-ray diffraction analysis for each sample synthesized. Subsequently the sample providing the highest magnetization was subjected to the detailed investigations. X-ray photoelectron spectroscopic investigation has assisted in ascertaining the presence of different valance states of nickel.

2. Experimental

2.1. Synthesis of $NiFe_2O_4$ nanoparticles

The nanoparticles of $NiFe_2O_4$, binary oxide were synthesized by gas phase condensation using Direct Current Transferred Arc Thermal Plasma Reactor (DCTATPR).

Table 1
Description of the different operating parameters and nomenclature of the samples.

Operating pressure (Torr)	Input plasma power (kW)	Sample name
250	3	NF_1(a)
	6	NF_1(b)
	8	NF_1(c)
500	3	NF_2(a)
	6	NF_2(b)
	8	NF_2(c)
760	3	NF_3(a)
	6	NF_3(b)
	8	NF_3(c)

In this process the plasma plume was made to strike the anode which consisted of an alloy of Ni and Fe prepared by mixing the micron sized powders of pure Ni and Fe and by forming pallets. These powders were mixed in the atomic weight ratio of 1:2 and palletized at 100 kg/cm^2 of pressure.

Fig. 1 shows the schematic diagram of the experimental setup used in DCTATPR. The pellets were placed over the water cooled graphite anode and were evaporated with the help of plasma, operated with an input power ranging between 3 and 8 kW. The plasma gas was argon; the flow of which through the torch was controlled at 5 L/min. The reacting gas was oxygen and purged at a rate of 20 L/min through the side port. The reactor chamber was evacuated by a rotary pump, to a base pressure of 10^{-2} Torr, before generating the plasma. However during synthesis the rate of evacuation was controlled to obtain a desired oxygen pressure which was monitored by a pressure gauge mounted on one of the ports.

As a result of the homogeneous gas phase condensation, particulates of reaction product were found to fly and get deposited over the water-cooled hemispherical dome. The collection criterion was so chosen that the particulates, before their deposition over the hemispherical dome, could travel almost equal distances from the plasma zone in order to suffer almost equal number of collisions. Sufficient time was allowed for the chamber to cool down to the ambient temperature after synthesis. This has helped in settling down the particulates over the reactor chamber walls.

In order to study the effect of operating pressure on the magnetic properties of the as-synthesized nanocrystalline $NiFe_2O_4$ powder, the synthesis was carried out at three different operating pressures viz. 250 Torr, 500 Torr and 760 Torr and the samples were named as NF_1, NF_2 and NF_3, respectively as shown in Table 1. In addition to the effect of operating pressure on the synthesized product, the effect of the input plasma power was also studied by varying the torch power from 3 kW to 8 kW for a given pressure.

The as synthesized powder, obtained at different parameters, was characterized by various techniques for determining the crystal structure, surface morphology, size and magnetic properties. The sample NF_2, which showed a high saturation magnetization, was further studied in details in order to understand the possible reasons for such enhanced properties, in spite of small particle sizes.

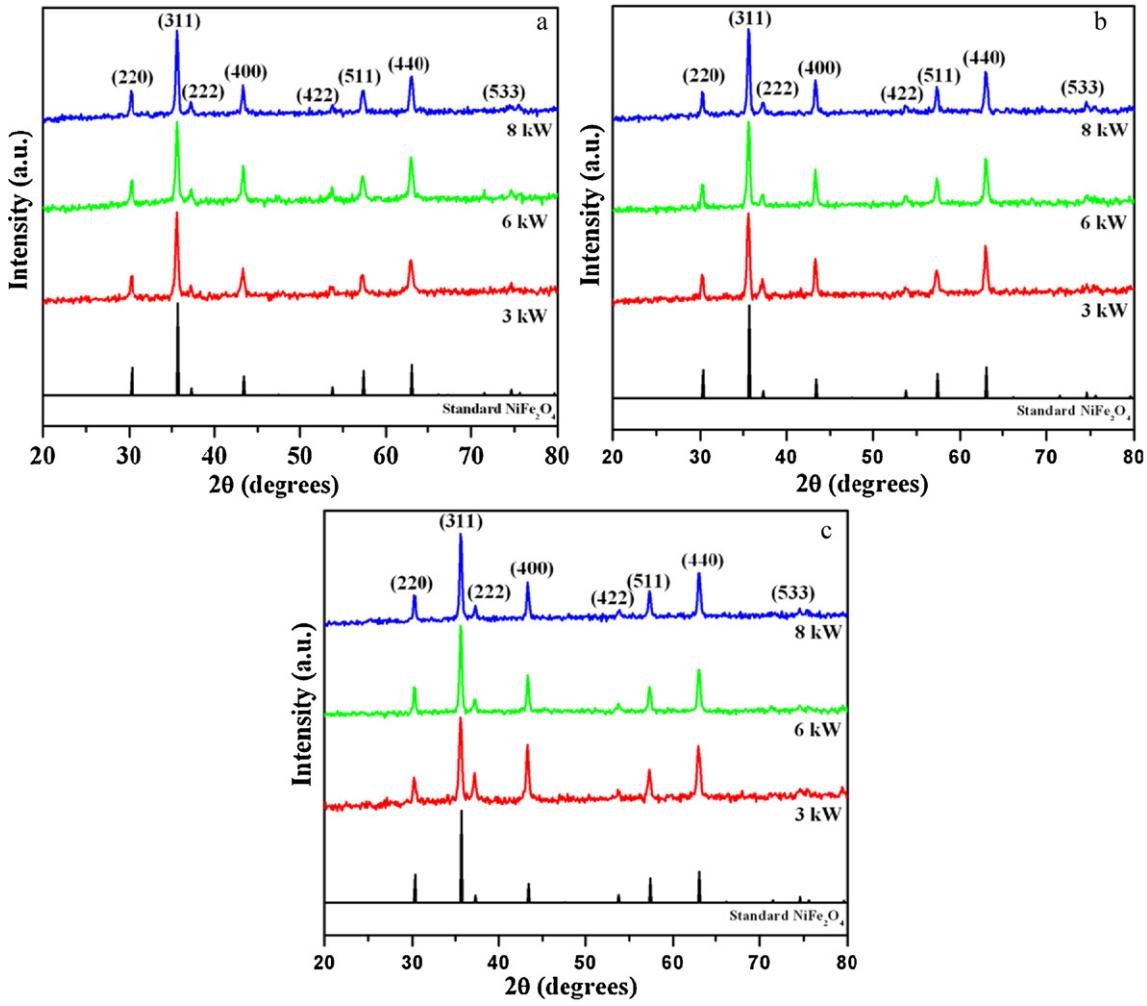

Fig. 2. XRD patterns of the as prepared $NiFe_2O_4$ synthesized at (a) 250 Torr, (b) 500 Torr and (c) 760 Torr with different input plasma powers.

2.2. Characterization

BRUKER AXS D8 ADVANCE X-ray diffractometer was used to record the X-ray diffraction pattern. The powder morphology and the crystalline structure were studied with the help of Transmission Electron Microscope (TEM) model PHILIPS CM200. The magnetic measurements were carried out using Vibrating Sample Magnetometer (VSM) model LakeShore 7307. Photoelectron spectra were recorded with V.G. Microtech ESCA 3000 (UK) spectrometer equipped with AlKα X-ray source ($h\nu$ = 1486.6 eV) and a hemispherical electron analyzer. The X-ray source was operated at 150 W. The residual pressure in the ion-pumped analysis chamber was maintained below 1.0×10^{-9} Torr during the data acquisition. The C_{1s} peak at the binding energy of 285 eV was taken as an internal standard. The accuracy of the binding energy values was within 0.2 eV.

3. Results and discussion

3.1. XRD analyses of $NiFe_2O_4$ nanoparticles

The as synthesized powder appeared brown in color. This was studied without any further post processing. XRD analysis was used to obtain the phase and crystalline properties of the sample. Fig. 2(a)–(c) shows the XRD patterns of the as collected samples of NF_1, NF_2 and NF_3. The standard line pattern of $NiFe_2O_4$, obtained from the JCPDS files (Card No. 74-2081), is presented at the bottom of each figure. The upper patterns correspond to the powder synthesized at different input powers viz. 3, 6 and 8 kW. Apart from the most intense line obtained at $2\theta = 35.6^\circ$ corresponding to (311) plane of $NiFe_2O_4$, other lines appeared at $2\theta = 30.3^\circ$, 37.2°, 43.3°, 53.8°, 57.3°, 62.9° and 74.6° corresponding to the ($h\,k\,l$) planes of (2 2 0), (2 2 2), (4 0 0), (4 2 2), (5 1 1), (4 4 0) and (5 3 3), respectively. These were seen to closely resemble the data for spinel cubic structure confirming the formation of crystalline phase of $NiFe_2O_4$. The absence of any additional lines, in any of the XRD patterns, confirms the purity of the $NiFe_2O_4$ phase in all the samples.

The average crystallite size 't' of the particles, in each case, was determined from the widths of the XRD lines using the Scherrer formula given by

$$t = \frac{0.9\lambda}{\beta \cos\theta} \quad (1)$$

where λ is the wavelength of X-rays, θ the Bragg angle and β the full width of the diffraction line at half of the maximum intensity. The average crystallite size was estimated to be around 28 nm among the different synthesized samples. This measurement points out towards the important information that the variation in the crystallite size is not very significant even though the reactor parameters are varied substantially. It may be, therefore, inferred that the crystallite size is less affected by the operating pressure and plasma currents during the synthesis in such a vapor phase condensation process using plasmas.

3.2. TEM micrograph of $NiFe_2O_4$ nanoparticles

The morphology, of the isolated non agglomerated particles, was investigated using the analysis of TEM micrographs. It was

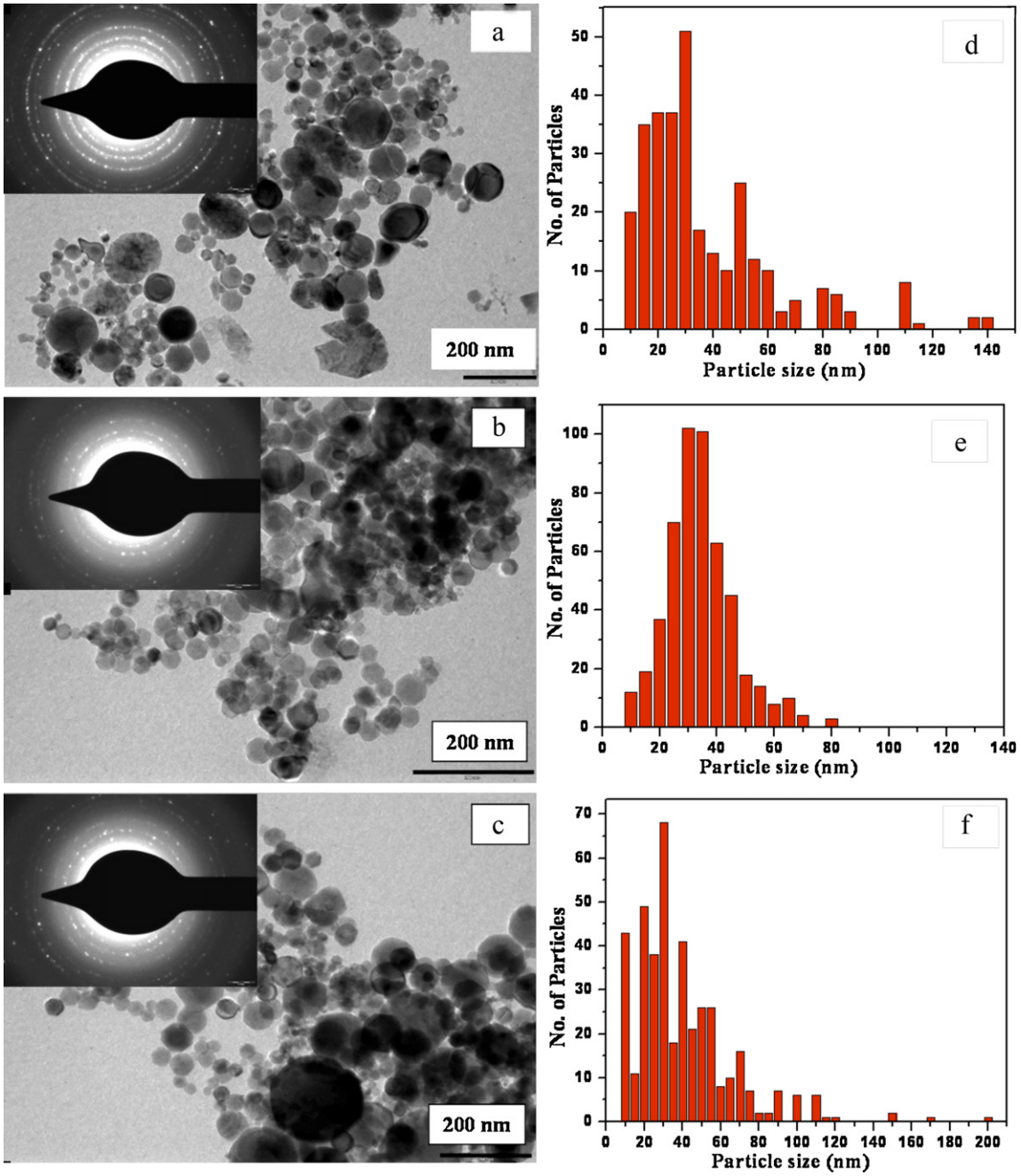

Fig. 3. (a)–(c) shows TEM micrographs along with the SAED pattern (shown in inset) and (d)–(f) shows the size histogram of samples NF_2(a), NF_2(b) and NF_2(c), respectively.

observed that the change in the particle size is insignificant, for all the samples studied. Fig. 3 shows the TEM images for the samples NF_2 which exhibits the spherical particles, with mean particle size around 30 nm. Corresponding histograms, showing the particle size distribution, are also presented. The inset shows the selected-area electron diffraction (SAED) pattern with clear ring structure confirming the presence of crystalline structure of $NiFe_2O_4$ when labeled with the corresponding ($h\,k\,l$) planes. The mean particle size (30 nm) estimated from TEM is in close agreement with the average crystallite size (28 nm) as calculated from XRD line broadening. This feature is quite important and points out towards the fact that the particles are highly crystalline in nature which is favorable for achieving high saturation magnetization.

3.3. Magnetic properties of $NiFe_2O_4$ nanoparticles

The magnetic properties of this nanostructured ferrite system were studied with the help of VSM. Fig. 4 shows the hysteresis loop of the samples NF_1, NF_2 and NF_3, respectively, at different input powers. The results provide the values of saturation magnetization, coercivity and remnant magnetization and are tabulated in Table 2 for all the samples studied. It is observed that the values of saturation magnetization of sample NF_1 ranges between 38 and 40 emu/g; for sample NF_2 it is in the range of 39–48 emu/g and for sample NF_3 it is around 34–37 emu/g. The reported value of the saturation magnetization, calculated using Neel's sub lattice theory for cubic inverse spinel $NiFe_2O_4$ is 50 emu/g [18] and reported value of the saturation magnetization experimentally observed for bulk

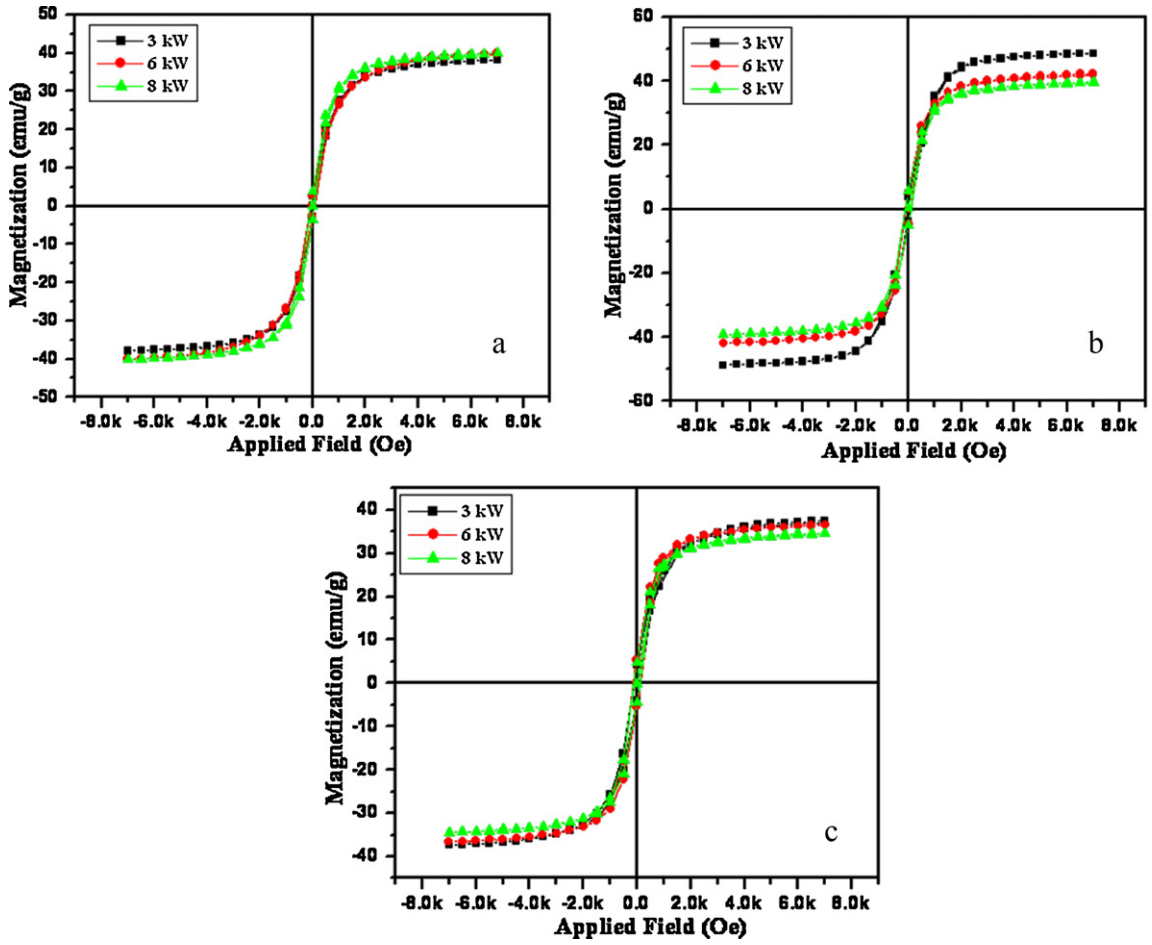

Fig. 4. Magnetization curves of the as prepared $NiFe_2O_4$ synthesized at (a) 250 Torr, (b) 500 Torr and (c) 760 Torr with different input plasma powers.

$NiFe_2O_4$ is 56 emu/g [27]. However, the saturation magnetization reported for nanoparticles of $NiFe_2O_4$ is lower than the bulk value and it is in the range of 7–23 emu/g for the particle size in the range of 20–30 nm [4,28–31]. Looking at the reported values of saturation magnetization of $NiFe_2O_4$, having particle size in the same range, the value in the present case for NF_2(a) is much higher than that of the reported one. Thus comparing with the values reported for the similar sizes of nanoparticles, the present value of 48 emu/g seems to be considerably high for nanoparticles. Large values of saturation magnetizations have been usually correlated [31] with the highest crystallinity of the nanoparticles. In the present case the particles are seen to possess high degree of crystallinity as discussed earlier while comparing the crystallite sizes obtained from XRD measurements with those of the particle sizes obtained from TEM analysis. This may be accounted to the high process temperature during the growth of nanocrystallites.

The values of the coercivity, as shown in Table 2 for the sample synthesized at different operating pressures are found to almost increase with increasing input power, except for NF_3. There might be different parameters which influence the value of coercivity in the ferrite systems. The size dependent variation in the coercivity has been well studied and a critical size has been put forward [16]. The coercivity value reaches maximum at the critical grain size and reduces both for the smaller and for the larger grain sizes. The critical grain size for the $NiFe_2O_4$ is 15 nm at 300 K [18]. Also the presence of defects, strains, magnetocrystalline anisotropy, shape anisotropy and surface spin disorder affects the coercivity of the magnetic materials [32–34]. Liu et al. [34] have reported the room temperature coercivity in $CoFe_2O_4$ particles as 5.1 kOe for the sample prepared by mechanical milling process. This large coercivity has been correlated to the high strain and defects produced in $CoFe_2O_4$ powders on account of the process of milling.

Table 2
Variation of magnetic properties for different operating parameters.

Sample name	Input plasma power (kW)	Magnetization M_s (emu/g)	Coercivity Hci (Oe)	Retentivity M_r (emu/g)
NF_1(a)	3	38.08	62.34	2.60
NF_1(b)	6	39.98	66.54	2.75
NF_1(c)	8	40.01	73.74	3.73
NF_2(a)	3	48.72	79.05	3.84
NF_2(b)	6	42.08	88.38	5.00
NF_2(c)	8	39.42	99.60	5.25
NF_3(a)	3	37.43	99.82	4.09
NF_3(b)	6	36.65	115.17	5.43
NF_3(c)	8	34.56	101.68	4.55

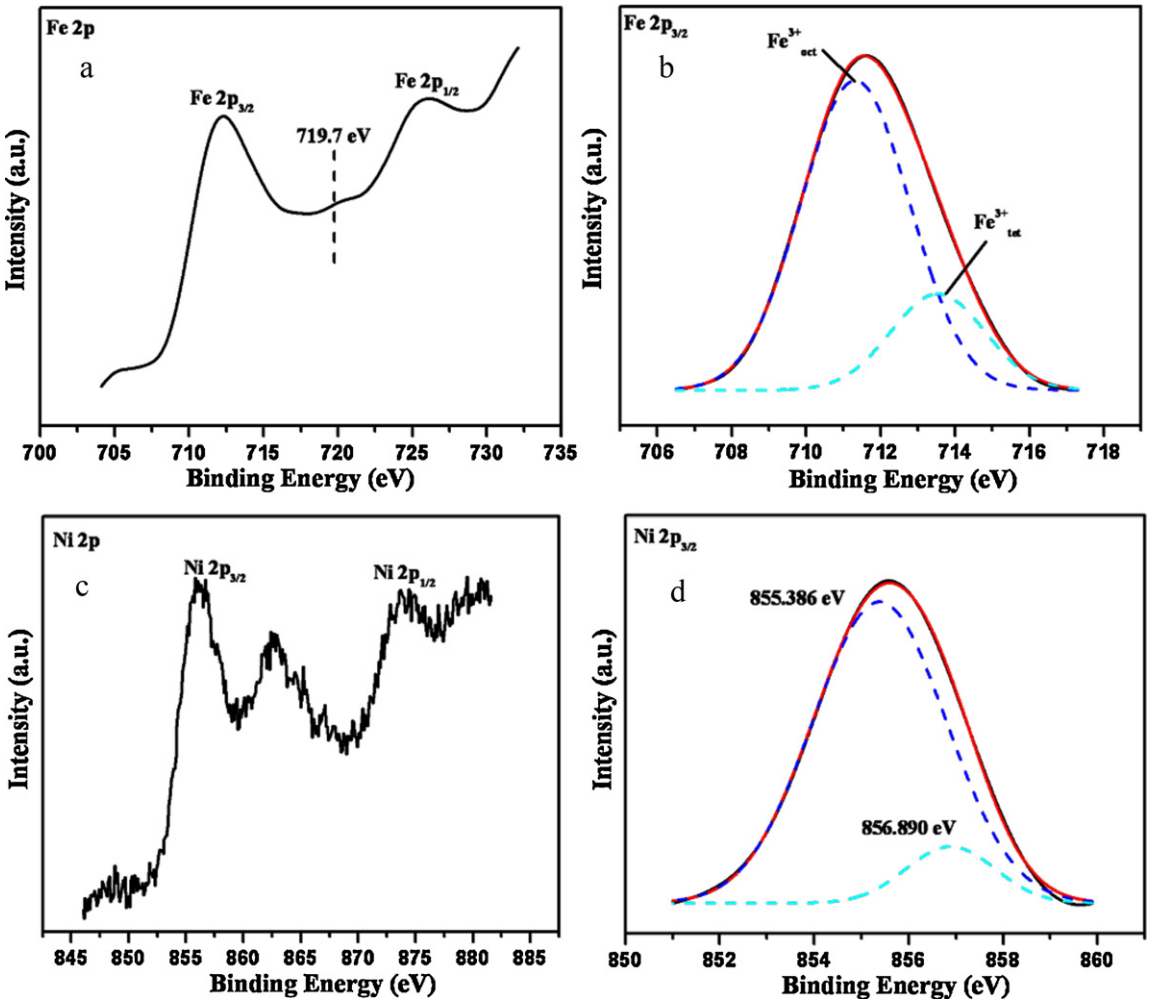

Fig. 5. Photoelectron spectra of NF_2(a) for (a) spectrum of Fe 2p in which the dotted line indicates the position of the satellite peak which confirms the absence of Fe^{2+} in the ferrites, (b) deconvoluted spectra of Fe $2p_{3/2}$ showing the presence of $Fe^{3+}{}_{oct}$ and $Fe^{3+}{}_{tet}$, (c) photoelectron spectra of Ni 2p and (d) deconvoluted spectra of the Ni $2p_{3/2}$ showing the presence of Ni^{2+} and Ni^{3+}.

Looking at the present values of coercivities and its variation with the operating parameters it may be fair to correlate the effects with the lattice defects present in the nanoparticles, since the particle size variation is not a systematic parameter. It is therefore less probable that the coercivity could be strongly linked with the variation in the particle size. The presence of lattice defects in the nanoparticles synthesized by vapor phase condensation cannot be ruled out because of the steep temperature gradient and high value of collisional rate. The observed increasing trend in the coercivity with the increasing operating pressure as well as plasma input power point out towards the increase in the defects centers arising in the ferrite crystals. This can be expected since the collision rate of particles will increase with increasing operating pressure as well as with increasing plasma power. In order to find the lattice defects in the as synthesized $NiFe_2O_4$, further investigations were carried out with a set of samples from NF_2. This was chosen because these samples exhibited higher saturation magnetization compared to the others. The elemental and stoichiometric compositions of NF_2 were investigated with the help of XPS analysis.

The effect of crystalline defects can also be highlighted by looking at the variation in the saturation magnetization with operating parameters. We observed that the overall variation in the magnetization shows a decreasing trend with increasing operating pressure and increasing plasma power. It is well documented that the saturated magnetization, in $NiFe_2O_4$, is related to various factors related to the defects such as cation redistribution, the existence of surface spins, formation of spin glass structures and the presence of NiO [3,22,27,31,35–37]. The fact that the XRD patterns do not indicate the presence of any oxide species apart from $NiFe_2O_4$, the possible lattice defects can arise from the cation redistribution alone. In order to understand the valance states of both cations, the samples were subjected to XPS analysis.

3.4. XPS analyses of $NiFe_2O_4$ nanoparticles

Figs. 5–7 show the XPS spectra for the set of samples NF_2(a), NF_2(b) and NF_2(c) synthesized at 3 kW, 6 kW, and 8 kW, respectively. Fig. 5(a) shows the XPS spectrum corresponding to Fe 2p photoelectron. The peak present at 711.32 eV with a small satellite peak at 8.4 eV above the main peak confirms the presence of Fe^{3+} in the sample [38,39]. The analysis of Fe $2p_{3/2}$ photoelectron peak for different chemical states of Fe is quite difficult due to the huge background. However the satellite peaks for Fe^{3+} and Fe^{2+} are found to be important. The Fe^{2+} $2p_{3/2}$ peak at 709.5 eV is always associated with a satellite peak at 6.0 eV above the principal peak where as Fe^{3+} $2p_{3/2}$ peak at 711.2 eV is associated with a satellite peak at 8.0 eV [40]. The difference in the satellite peaks of the Fe^{3+} and Fe^{2+} is due to two final states caused by photoemission of Fe. As Fe^{2+} and Fe^{3+} have d^6 and d^5 states, respectively, in the valance band; the satellite peak appears at different positions during the

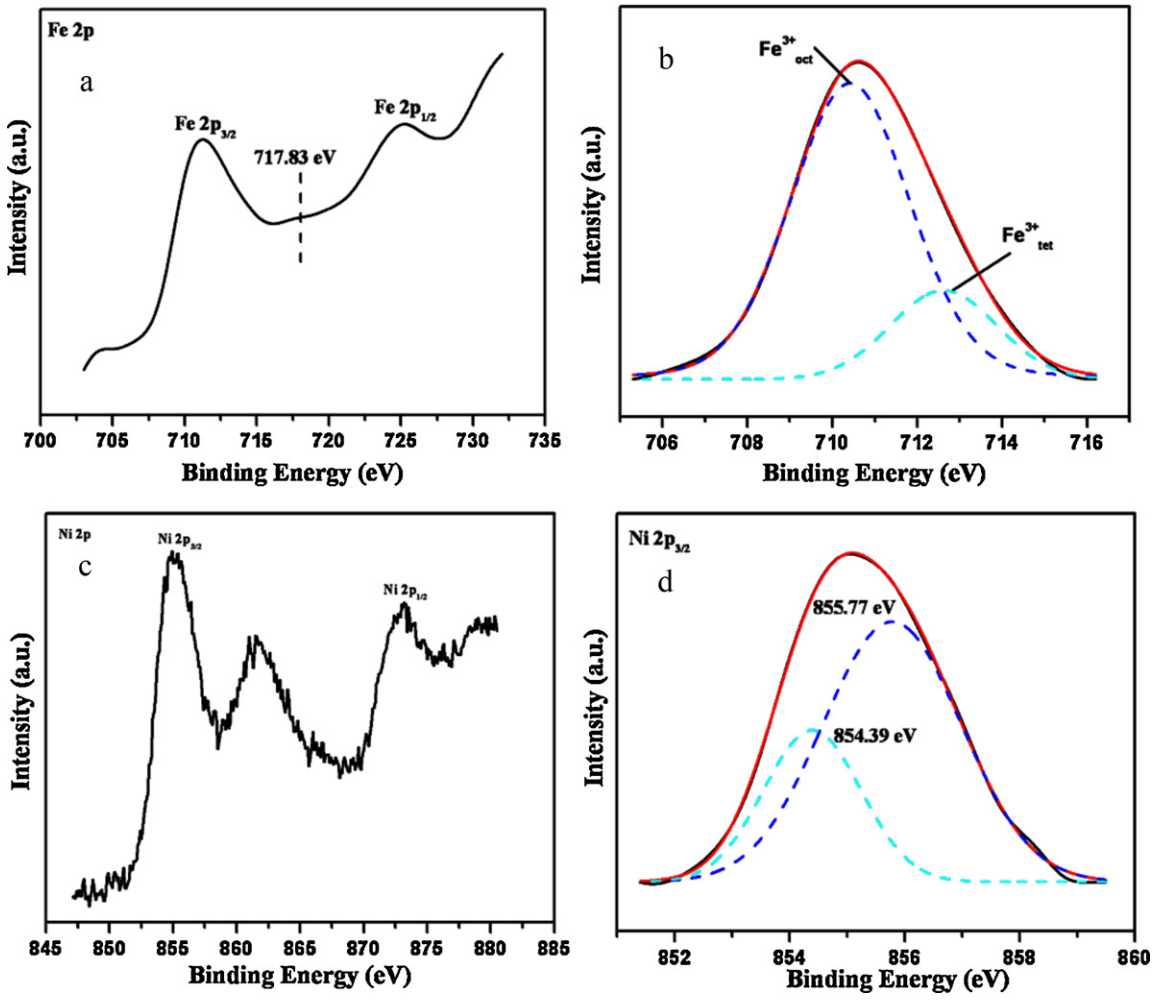

Fig. 6. Photoelectron spectra of NF_2(b) for (a) spectrum of Fe 2p in which the dotted line indicates the position of the satellite peak which confirms the absence of Fe^{2+} in the ferrites, (b) deconvoluted spectra of Fe $2p_{3/2}$ showing the presence of $Fe^{3+}{}_{oct}$ and $Fe^{3+}{}_{tet}$, (c) photoelectron spectra of Ni 2p and (d) deconvoluted spectra of the Ni $2p_{3/2}$ showing the presence of Ni^{2+} and Ni^{3+}.

relaxation of the metal ion and is observed to be characteristic of the oxidation state of the iron. The deconvolution of Fe $2p_{3/2}$ peak, showed in Fig. 5(b), provides two peaks at around 711.32 eV and 713.54 eV. Zhang et al. [39] have reported that the deconvolution of Fe $2p_{3/2}$ region shows that the Fe^{3+} species exist in tetrahedral and octahedral sites. The tetrahedral, $Fe^{3+}{}_{tet}$, is at the higher binding energy and the octahedral, $Fe^{3+}{}_{oct}$, is at the lower binding energy. Fig. 5(c) shows Ni 2p photoelectron spectra of the as prepared sample. The deconvolution of the Ni $2p_{3/2}$ peak [Fig. 5(d)] results into two peaks at around 855.3 eV and 856.8 eV which are attributed to the Ni^{2+} and Ni^{3+} states of Ni at the octahedral and tetrahedral sites, respectively [41].

Similarly Figs. 6 and 7 describe the experimental results corresponding to NF_2(b) and NF_2(c) prepared at 6 and 8 kW of plasma power, respectively. The corresponding binding energies and the correlated valance states of species are listed in Table 3. The table summarizes all the values of binding energies in eV for different species and their correlation to the reported literature [38–41]. Presence of Ni^{3+} along with Ni^{2+} is normally unusual in case of nickel ferrite and thus requires further analysis.

3.5. Analysis of possible cation distribution for $NiFe_2O_4$

Using this information of XPS data, the possible cation distribution was inferred from the relative integrated intensity calculations from the XRD data. As suggested by Buerger [42], the relative integrated intensity of the XRD lines can be calculated using the formula:

$$I_{hkl} = |F|^2 P L_p \tag{2}$$

where F is the structure factor, P is the multiplicity factor and L_p is the Lorentz-polarization factor which depends only on the Bragg diffraction angle θ,

$$L_p = \frac{1 + \cos^2 2\theta}{\sin^2 2\theta} \tag{3}$$

Intensity ratios I_{220}/I_{222}, I_{220}/I_{400}, I_{220}/I_{422} and I_{422}/I_{400} corresponding to various lines in the XRD pattern of the spinel structure are found to be sensitive to the cation distributions on account of the structure factor [27,36]. $NiFe_2O_4$ consists of spinel structure where in Ni^{2+} occupies the octahedral site and Fe^{3+} occupies the octahedral as well as tetrahedral sites. The intensities of these lines were calculated using Eq. (2) by considering all possible cation distributions of Ni^{2+}, Ni^{3+} and Fe^{3+} ions in both tetrahedral and octahedral sites. For various cation distributions the relative intensity ratios were calculated and compared with the experimentally observed intensity ratios. The oxygen positional parameter was chosen to be 0.375. Finally, the cation distribution for which the calculated and observed intensity ratios closely matched with each other and the magnetic moment per formula unit calculated by Neel's theory

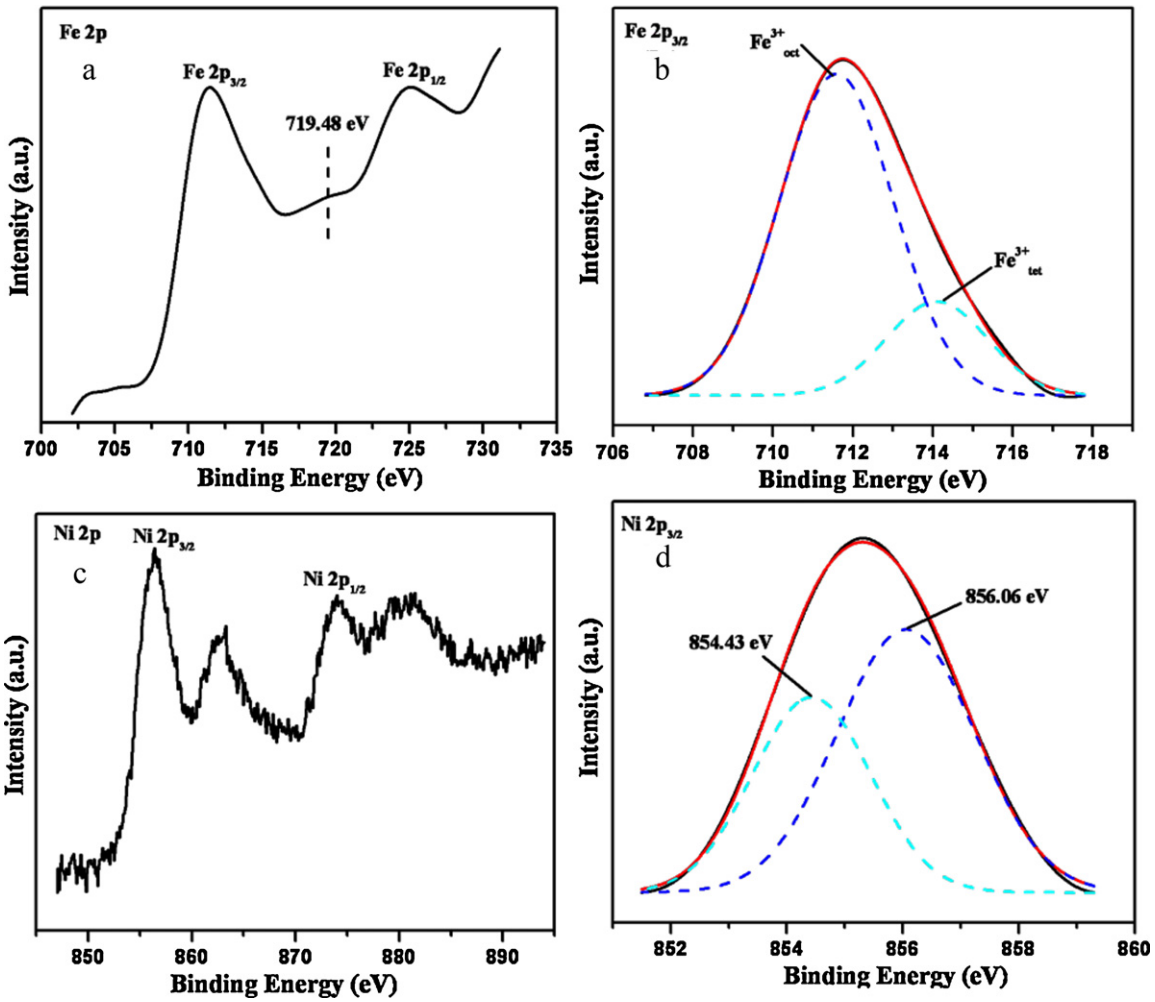

Fig. 7. Photoelectron spectra of NF_2(c) for (a) spectrum of Fe 2p in which the dotted line indicates the position of the satellite peak which confirms the absence of Fe^{2+} in the ferrites, (b) deconvoluted spectra of Fe $2p_{3/2}$ showing the presence of $Fe^{3+}{}_{oct}$ and $Fe^{3+}{}_{tet}$, (c) photoelectron spectra of Ni 2p and (d) deconvoluted spectra of the Ni $2p_{3/2}$ showing the presence of Ni^{2+} and Ni^{3+}.

matched closely with the experimentally observed magnetic values was taken as a correct distribution.

As a result, the cation distribution and the corresponding relative intensities of experimental and calculated XRD lines are listed in Table 4, where, the parentheses and the brackets represent tetrahedral and octahedral sites, respectively. It was observed that in all the samples, Ni^{3+} ions were present at the tetrahedral site by replacing the same amount of the Fe^{3+} from the tetrahedral site. Reports in the literature suggest that in case of nanocrystalline $NiFe_2O_4$, part of the Ni^{2+} can occupy the tetrahedral site, which otherwise occupies the octahedral site. Shafer [43] suggested that the single phase nickel–iron spinels having excess nickel (Ni^{3+} ions in addition to Ni^{2+} ions) replaces the Fe^{3+} ions. He has used an amorphous material of iron and nickel oxide which was prepared by either co-precipitating the hydroxides of iron and nickel or by forming a gel from an alcoholic solution and then vacuum drying at low temperatures. He has reported that the solubility of excess Ni increases with increasing oxygen pressure during sintering. In the present studies fraction of excess Ni^{2+} ions occupies octahedral site by substituting part of Fe^{3+} ions on octahedral site along with small fraction of

Table 3
Binding energies of Fe $2p_{3/2}$ and Ni $2p_{3/2}$ photoelectron peaks measured for sample NF_2 at different input plasma powers.

Species	Sample name	Binding energy (eV)	Probable valance states	References
Fe $2p_{3/2}$	NF_2(a)	711.3	$Fe^{3+}{}_{oct}$	[38,39]
		713.5	$Fe^{3+}{}_{tet}$	
	NF_2(b)	710.4	$Fe^{3+}{}_{oct}$	
		712.6	$Fe^{3+}{}_{tet}$	
	NF_2(c)	711.5	$Fe^{3+}{}_{oct}$	
		714.1	$Fe^{3+}{}_{tet}$	
Ni $2p_{3/2}$	NF_2(a)	855.3	Ni^{2+}	[41]
		856.8	Ni^{3+}	
	NF_2(b)	854.3	Ni^{2+}	
		855.7	Ni^{3+}	
	NF_2(c)	854.4	Ni^{2+}	
		856.0	Ni^{3+}	

Table 4
The XRD cation distribution values in $NiFe_2O_4$ for the sample NF_2 synthesized at different input plasma powers.

Sample name	Cation distribution	$I(220)/I(222)$		$I(220)/I(400)$		$I(422)/I(400)$	
		Obs.	Cal.	Obs.	Cal.	Obs.	Cal.
NF_2(a)	$(Fe^{3+}_{0.9}\ Ni^{3+}_{0.1})\ [Ni^{2+}_{1.333}\ Fe^{3+}_{0.9}]$	1.43	1.79	0.65	0.74	0.17	0.25
NF_2(b)	$(Fe^{3+}_{0.9}\ Ni^{3+}_{0.1})\ [Ni^{2+}_{1.165}\ Fe^{3+}_{0.9}]$	1.97	2.47	0.67	0.85	0.25	0.29
NF_2(c)	$(Fe^{3+}_{0.9}\ Ni^{3+}_{0.1})\ [Ni^{2+}_{1.14}\ Fe^{3+}_{0.9}]$	2.01	2.52	0.75	1.09	0.23	0.37

Table 5
The magnetic moment per formula unit for sample NF_2 synthesized at different input plasma powers.

Sample name	Cation distribution	Saturation magnetization M_s (emu/g) (VSM)	Magneton number n_B (μ_B)	
			Obs. (VSM)	Cal. (XRD)
NF_2(a)	$(Fe^{3+}_{0.9}\ Ni^{3+}_{0.1})\ [Ni^{2+}_{1.333}\ Fe^{3+}_{0.9}]$	48.79	2.04	2.36
NF_2(b)	$(Fe^{3+}_{0.9}\ Ni^{3+}_{0.1})\ [Ni^{2+}_{1.165}\ Fe^{3+}_{0.9}]$	42.03	1.76	2.03
NF_2(c)	$(Fe^{3+}_{0.9}\ Ni^{3+}_{0.1})\ [Ni^{2+}_{1.14}\ Fe^{3+}_{0.9}]$	39.46	1.65	1.98

Ni^{2+} ions as excess content. Presence of excess Ni^{3+} at the tetrahedral site in place of Fe^{3+} ion in the tetrahedral site is also observed. The decrease in the saturation magnetization with increasing input plasma power during synthesis indicates that the presence of the excess Ni^{2+} at the octahedral site plays an important role. Thus all the samples are found to be iron deficit and nickel rich.

Using the value of saturation magnetization at room temperature, the magnetic moment per formula unit in Bohr magneton 'μ_B' is calculated by the following equation [36]:

$$n_B = \frac{M\,wt \times M_s}{5585} \quad (4)$$

The magnetic moment per formula unit in Bohr magneton was also calculated according to the Neel's ferrimagnetic theory as,

$$n_B = M_B - M_A \quad (5)$$

where M_A and M_B are the magnetic moments in Bohr magneton (μ_B) for A and B sites.

The magnetic moments for Fe^{3+}, Ni^{3+} and Ni^{2+} ions are 5, 3, and 2 μ_B, respectively, which are used in the present calculations. The results are summarized in Table 5.

For the complete inverse spinel structure of $NiFe_2O_4$; the net magnetization is due to the presence of Ni^{2+} in B site only, since the moments of Fe^{3+} ions from A and B sites cancel each other. In the present case we have observed that a few A sites of Fe^{3+} are occupied by the Ni^{3+} species and also a few B sites of Fe^{3+} are occupied by Ni^{2+} and thus the iron deficit $NiFe_2O_4$ is formed. The presence of Ni^{3+} in A site and also excess of small Ni^{2+} in B site enhances the net saturation magnetization. The percentage of Ni^{3+} at A site in all the samples (NF_2(a) to NF_2(c)) is same and hence it has contributed equally in the enhancement of magnetization in all the samples. However, the percentage of Ni^{2+} is seen to decrease with increasing power and thus its net effect on the saturation magnetization is to decrease it with the increasing plasma power. The sample NF_2(a), therefore, shows the higher saturation magnetization than the other samples. It is observed that the calculated values of n_B are comparable to those of the experimental values which explain the higher value of saturation magnetization in NF_2(a).

4. Conclusions

In summary the magnetic nanoparticles of $NiFe_2O_4$ have been successfully synthesized by DCTATPR using pellets of commercially available coarse grain powders of Ni and Fe. The as synthesized nanoparticles of $NiFe_2O_4$ are found to be polycrystalline in nature with average particle size of 30 nm, as revealed by the TEM analysis. The saturation magnetization and coercivty values of the as synthesized particles were found to be dependent on the different operating parameters. The highest value of saturation magnetization at room temperature was observed at 500 Torr of operating pressure with 3 kW of input power and highest coercivity at room temperature was observed at 760 Torr of operating pressure with 6 kW of input power. XPS study has conclusively established the presence of Fe^{3+} species in both octahedral and tetrahedral sites and the presence of Ni^{3+} species along with Ni^{2+} in the as synthesized $NiFe_2O_4$ nanoparticles. The magnetic properties of $NiFe_2O_4$ are, thus, seen to be influenced by the change in the plasma parameters on account of the cation distributions.

Acknowledgements

The authors acknowledge BRNS (DAE) India for funding the research project. A.B.N. expresses his thanks to BARC (DAE) India for providing a research fellowship under the MOU programme. S.V.B. thanks the Council of Scientific and Industrial Research, India for providing the ES scheme.

References

[1] S. Maensiri, C. Masingboon, B. Boonchom, S. Seraphin, Scripta Mater. 56 (2007) 797–800.
[2] D. Carta, D. Loche, G. Mountjoy, G. Navarra, A. Corrias, J. Phys. Chem. C 112 (2008) 15623–15630.
[3] Y. Kinemuchi, K. Ishizaka, H. Suematsu, W. Jiang, K. Yatsui, Thin Solid Films 407 (2002) 109–113.
[4] M.N.B. Silva, J.G. dos, S. Duque, D.X. Gouveia, J.A.C. de Paiva, M.A. Macedo, Jpn. J. Appl. Phys. 43 (2004) 5249.
[5] R.J. Munz, T. Addona, A.C. Da Cruz, Pure Appl. Chem. 71 (1999) 1889–1897.
[6] R.G. Reddy, L.V.M. Antony, J. Met. 55 (2003) 19–22.
[7] C Balasubramaniam, Y.B. Khollam, I. Banerjee, P.P. Bakare, S.K. Date, A.K. Das, S.V. Bhoraskar, Mater. Lett. 58 (2004) 3958–3962.
[8] I. Banerjee, Y.B. Khollam, C. Balasubramaniam, R. Pasricha, P.P. Bakare, K.R. Patil, A.K. Das, S.V. Bhoraskar, Scripta Mater. 54 (2006) 1235–1240.
[9] H. Nagar, N.V. Kulkarni, S. Karmakar, B. Sahoo, I. Banerjee, P.S. Chaudhari, R. Pasricha, A.K. Das, S.V. Bhoraskar, S.K. Date, W. Keune, Mater. Character 59 (2008) 1215–1220.
[10] N.V. Kulkarni, S. Karmakar, I. Banerjee, S.N. Sahasrabudhe, A.K. Das, S.V. Bhoraskar, Mater. Res. Bull. 44 (2009) 581–588.
[11] K.V.P.M. Shafi, Y. Koltypin, A. Gedanken, J. Phys. Chem. B 101 (1997) 6409–6414.
[12] S. Prasad, N.S. Gajbhiye, J. Alloys Compd. 265 (1998) 87–92.
[13] J.M. Yang, W.J. Tsuo, F.S. Yen, J. Solid State Chem. 145 (1999) 50–57.
[14] A.H. Morrish, K. Haneda, J. Appl. Phys. 52 (1981) 2496–2498.
[15] D.H. Chen, Y.Y. Chen, J. Colloid Interface Sci. 9 (2001) 235.
[16] Y. Shi, J. Ding, X. Liu, J. Wang, J. Magn. Magn. Mater. 205 (1999) 249–254.
[17] D.H. Chen, X.R. He, Mater. Res. Bull. 36 (2001) 1369–1377.
[18] M. George, A.M. John, S.S. Nair, P.A. Joy, M.R. Anantharaman, J. Magn. Magn. Mater. 302 (2006) 190–195.
[19] W. Jiang, K. Yatsui, IEEE Trans. Plasma Sci. 26 (1998) 1498–1501.
[20] J. Liu, H. He, X. Jin, Z. Hao, Z. Hu, Mater. Res. Bull. 36 (2001) 2357–2363.
[21] A. Kale, S. Gubbala, R.D.K. Misra, J. Magn. Magn. Mater. 277 (2004) 350–358.
[22] R.D.K. Misra, S. Gubbala, A. Kale, W.F. Egelhoff Jr., Mater. Sci. Eng. B 111 (2004) 164–174.

[23] J. Zhou, J. Ma, C. Sun, L. Xie, Z. Zhao, H. Tian, J. Am. Ceram. Soc. 88 (2005) 3535–3537.
[24] L.J. Cote, A.S. Teja, A.P. Wilkinson, Z. Zhang, J. Fluid Phase Equilib. 210 (2003) 307–317.
[25] S. Komerneni, M.C. D'Arrigo, C. Leonelli, G.C. Pellacani, H. Katsuki, J. Am. Ceram. Soc. 81 (1998) 3041–3043.
[26] P.E. Meskin, V.K. Ivanov, A.E. Barantchikov, B.R. Churagulov, Y.D. Tretyakov, Ultrason. Sonochem. 13 (2006) 47–53.
[27] V. Sepelak, K. Tkacova, V.V. Boldyrev, S. Wibmann, K.D. Becker, Physica B 617 (1997) 234–236.
[28] V. Sepelak, M. Menzel, I. Bergmann, M. Wiebcke, F. Krumeich, K.D. Becker, J. Magn. Magn. Mater. 272 (2004) 1616–1618.
[29] J.H. Liu, L. Wang, F.S. Li, J. Mater. Sci. 40 (2005) 2573–2575.
[30] M.S. Niasari, F. Davar, T. Mahmoudi, Polyhedron 28 (2009) 1455–1458.
[31] S. Chkoundali, S. Ammar, N. Jouini, F. Fievet, P. Molinie, M. Danot, F. Vallain, J.M. Greneche, J. Phys. Condens. Matter. 16 (2004) 4357–4372.
[32] M.L. Limaye, S.B. Singh, S.K. Date, D. Kothari, V.R. Reddy, A. Gupta, V. Sathe, R.J. Chaudhary, S.K. Kulkarni, J. Phys. Chem. B 113 (2009) 9070–9076.
[33] Y.C. Wang, J. Ding, J.B. Yi, B.H. Liu, T. Yu, Z.X. Shen, Appl. Phys. Lett. 84 (2004) 2596–2598.
[34] B.H. Liu, J. Ding, Z.L. Dong, C.B. Bothroyd, J.H. Yin, J.B. Yi, Phys. Rev. B 74 (2006), 184427(1–10).
[35] H. Nathani, S. Gubbala, R.D.K. Misra, Mater. Sci. Eng. B 111 (2004) 95–100.
[36] H. Kavas, A. Baykal, M.S. Topark, Y. Koseoglu, M. Sertkol, B. Aktas, J. Alloys Compd. 479 (2009) 49–55.
[37] C.N. Chinnasamy, A. Narayannasamy, N. Ponpandian, K. Chatopadhyay, K. Shinoda, B. Jeyaadevan, K. Tohji, K. Nakatsuka, T. Furubayashi, I. Nakatani, Phys. Rev. B 63 (2001), 184108(1–6).
[38] F. Li, X.F. Liu, Q.Z. Yang, J.J. Liu, D.G. Evans, X. Duan, Mater. Res. Bull. 40 (2005) 1244–1255.
[39] J. Zhang, J. Shi, M. Gong, J. Solid State Chem. 182 (2009) 2135–2140.
[40] V.K. Mittal, P. Chandramohan, S. Bera, M.P. Srinivasan, S. Velmurugan, S.V. Narasimhan, Solid State Commun. 137 (2006) 6–10.
[41] B. Baruwati, R.K. Rana, S.V. Manorama, J. Appl. Phys. 101 (2007), 014302(1–7).
[42] M.J. Buerger, Crystal Structure Analysis, Wiley Interscience, New York, 1960, pp. 35.
[43] M.W. Shafer, J. Appl. Phys. 33 (Suppl.) (1962) 1210–11211.